Theoretical investigation of the defect formation mechanism relevant to nonstoichiometry in hydroxyapatite

Katsuyuki Matsunaga
Department of Materials Science and Engineering, Kyoto University Yoshida-Honmachi, Sakyo, Kyoto, 606-8501, Japan
(Received 31 August 2007; revised manuscript received 22 November 2007; published 10 March 2008)

Electronic and atomic structures of vacancies and protons in hydroxyapatite (HAp) are analyzed by using first-principles band structure calculations. From total energies of supercells for monoclinic HAp, defect formation energies and equilibrium concentrations are evaluated, assuming chemical equilibrium between HAp and aqueous solution saturated with respect to HAp. It is found that interstitial and Ca-substitutional protons form H_2O groups or acid phosphates of HPO_4^{2-} and are stabilized by making hydrogen bonding with adjacent PO_4^{3-} groups. Moreover, defect association considerably decreases the defect formation energies, and, in particular, interstitial protons bonded to OH^- groups become most stable when associated with Ca-substitutional protons. Due to abundant formation of the associated defect comprising interstitial and Ca-substitutional protons, Ca contents in HAp decrease with lowering pH, which explains pH dependence of Ca/P molar ratios of HAp observed experimentally.

DOI: 10.1103/PhysRevB.77.104106 PACS number(s): 61.72.J−, 71.15.Mb

I. INTRODUCTION

Hydroxyapatite [HAp, $Ca_5(PO_4)_3OH$] is expected as biocompatible materials, and its chemistry and defect structures are of considerable importance in unraveling biological phenomena occurring in human bones and teeth. It is known that HAp components in human bodies are usually nonstoichiometric and also contain a variety of impurities.[1,2] A Ca/P molar ratio in naturally occurring and/or experimentally prepared HAp, which is 1.67 in the stoichiometric case, varies from 1.5 to 1.67 (Ca deficient), depending on the surrounding chemical and experimental environments.[1] Since biological properties of HAp should be closely related to the nonstoichiometry, it is necessary to clarify a mechanism of point defect formation in HAp, especially at low temperatures and in aqueous solution as encountered in human bodies.

A number of mechanisms for point-defect formation in Ca-deficient HAp were proposed, which were based on experimental chemical analyses for HAp crystals prepared by low-temperature processes such as solution precipitation.[2–9] In the mechanisms, incorporation of protons that occurs from aqueous solutions surrounding HAp crystals is responsible for the nonstoichiometry. Posner *et al.* and their co-workers suggested that the Ca deficiency is due to Ca^{2+} vacancies charge compensated by two protons, where the chemical formula is represented as $Ca_{10-x}H_{2x}(PO_4)_6(OH)_2$.[2–4] It is noted here that the charge-compensating protons are considered to be located between oxygen atoms of two adjacent PO_4^{3-} groups, namely, in the form of protonated PO_4^{3-} (HPO_4^{2-}). Winand *et al.* pointed out formation of OH^- vacancies, and took into account charge compensation among Ca^{2+} vacancies, OH^- vacancies, and protons, which results in the chemical formula of $Ca_{10-x}(HPO_4)_x(PO_4)_{6-x}(OH)_{2-x}$.[5,6] This mechanism was also supported by Bery.[7,8] The chemical formula of Ca-deficient HAp proposed by Kuhl and Nebergall[9] is similar to the one of Winand *et al.*,[5,6] but arises from two independent charge-compensation mechanisms: (a) a pair of Ca^{2+} and OH^- vacancies with one charge-compensating proton and (b) two OH^- vacancies with one Ca^{2+} vacancy. The defect-formation mechanisms at a low temperature would also be important for HAp in human bodies, because successive dissolution and reprecipitation processes of HAp always takes place in body fluids, leading to the observed nonstoichiometry. Therefore, an understanding of the defect-formation mechanism of pure HAp is an essential step to reveal properties and phenomena of biological HAp involved in human bodies.

As stated above, the point-defect chemistry of HAp is complex, which prevents further understanding of physical and chemical properties of HAp in biological environment. In this regard, recent first-principles calculations have a great possibility to provide a detailed mechanism of point defect formation in oxides theoretically. This is also the case for HAp, and there have been a number of first-principles calculations for HAp with/without defects. Calderín *et al.*[10] and Rulis *et al.*[11] performed first-principles band structure calculations to investigate atomic arrangement and bonding characteristics in bulk HAp. In contrast, Ellis and co-workers calculated substitutional defects of CO_2, Fe, and Zn in HAp by using cluster models, and made comparison with available experimental data to identify characteristic electronic structures localized around the defects.[12–14] More recently, Astala *et al.* performed first-principles pseudopotential calculations for substitutional CO_3 and Si in HAp.[15,16] The authors evaluated the relative defect formation energies, and investigated the charge-compensation mechanism energetically most favorable. Previously, we also studied intrinsic vacancies in HAp, and examined temperature dependence of the vacancy formation energies, which successfully explains dehydration behavior of HAp observed experimentally.[17] However, a dominant defect reaction occurring in HAp in aqueous solutions has not been theoretically addressed.

In the present study, first-principles calculations are performed to study atomic and electronic structures of intrinsic vacancies and protons in HAp. Based on total energies by supercell calculations, defect formation energies in equilibrium between HAp and its saturated aqueous solution are quantitatively evaluated. For this purpose, chemical poten-

tials of individual ionic species in the solution at a particular pH condition are defined according to thermodynamic treatments with the aid of experimental and first-principles data. Details of the present first-principles approach to defect chemistry in the solid-liquid equilibrium will be described in Sec. II. Characteristics of electronic density of states and optimized atomic structures around vacancies and protons in HAp will be shown in Secs. III A and III B. Finally, formation energies of isolated and associated defects are quantitatively evaluated in Sec. III C, and then possible defect reactions giving rise to the observed nonstoichiometry of HAp will be discussed.

II. COMPUTATIONAL PROCEDURE

A. Electronic structure calculation and supercell

First-principles electronic structure calculations are performed based on the projector augmented wave (PAW) method, which is implemented in the Vienna *ab initio* simulation package.[18–21] The generalized gradient approximation is used for the exchange-correlation potential proposed by Perdew, Bruke, and Ernzerhof.[22] A plane-wave cutoff energy (E_{cut}) is set at 500 eV throughout the present study. Structural relaxation is carried out for all atoms in a unit cell and supercells, and is truncated when the atomic forces are less than 0.05 eV/Å.

In this study, point defects in HAp with a monoclinic structure[23] ($P2_1/b$) are investigated. The monoclinic structure is similar to the hexagonal one,[24] and the unit cell (88 atoms) can be described as the hexagonal unit (44 atoms) doubled along the b axis, where the OH columns in the $\pm c$ axis directions are alternatively arranged (see Fig. 1). According to the designation by Elliot *et al.*,[23] five different Ca sites (Ca-1, Ca′-1, Ca-2a, Ca-2b, and Ca-2c), three P sites (P-a, P-b, and P-c), thirteen O sites (O-1a, O-1b, O-1c, O-2a, O-2b, O-2c, O-3a, O-3b, O-3c, O′-3a, O′-3b, O′-3c, and O-h), and a hydrogen site adjacent to O-h (forming OH^- group) are involved in the unit cell. The Ca-1 and Ca′-1 atoms are generally referred to as columnar Ca, and are sixfold coordinated by oxygen atoms at the vertices of adjacent PO_4^{3-} tetrahedra with an average interatomic distance of 0.244 nm (see also Table I). On the other hand, the Ca-2abc atoms (triangular Ca) form triangles around the OH columns along the c axis, and the two adjacent Ca-2 triangles are rotated by 60° about the OH^- column from each other.[1] The triangular Ca atoms are also sixfold coordinated by oxygen atoms with an average bond length of 0.242 nm, but one of the coordinating O atoms belongs to OH^- group.

The m-HAp structure was first calculated on the $2\times1\times3$ k-point mesh generated by the Monkhorst-Pack (MP) scheme (four irreducible k points).[25] The optimized lattice parameters were $a=0.952$ nm, $b=2a$, and $c=0.691$ nm, which agrees well with experiment ($a=0.942$ nm, $b=2a$, and $c=0.688$ nm).[23]

Based on the unit-cell structure thus calculated, supercells of m-HAp are generated by doubling the unit cell along the a and c axes, so that the total number of atoms in the perfect supercell is 352. In the supercell calculations, Brillouin zone sampling is done only at the Γ point because of the rather large supercell. For calculations of vacancies (interstitials) in m-HAp, ions or ion groups of interest are removed from (added to) the perfect supercell, and all atoms in the supercells were allowed to relax in the manner described above. In order to check the computational accuracy in the present supercell calculations, test calculations in more severe conditions of $E_{\mathrm{cut}}=550$ eV or two irreducible k points are carried out for supercells with/without a Ca vacancy. It is confirmed that the total energy convergence is less than 1.5 meV/atom, which results in a difference in defect formation energy of less than 0.02 eV.

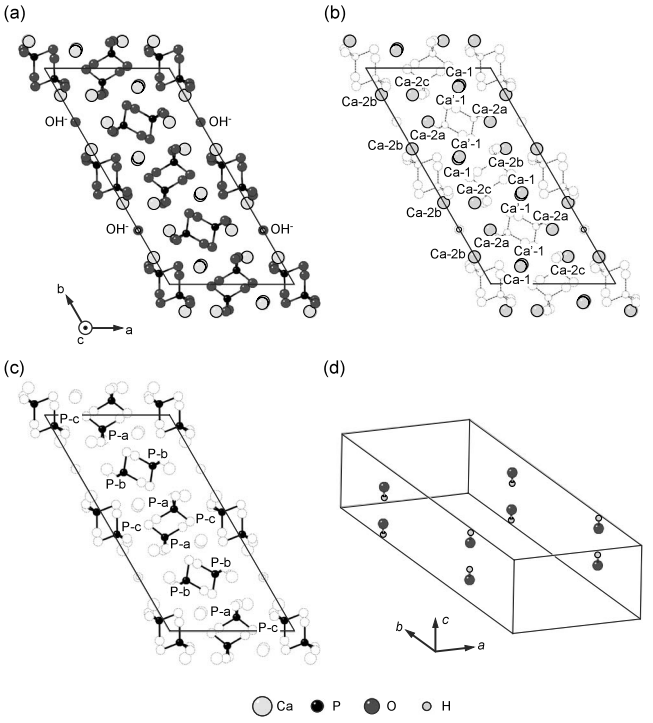

FIG. 1. Crystal structure of monoclinic HAp. (a), (b), and (c) are illustrations viewed along the c axis, and atomic positions of Ca and P are highlighted in (b) and (c), respectively. In (d), only OH groups are drawn to show the alternate arrangement of the OH columns in the $\pm c$-axis directions.

B. Defect formation energy

In this study, intrinsic vacancies, interstitial and substitutional protons in m-HAp are considered, and their energetics is investigated by first-principles calculations with a supercell technique. Defect formation energies (ΔH_{f}) are evaluated from total energies (E_{T}) of the perfect and defective supercells. When a defect with charge q is formed by addition or removal of an atom α and electrons in HAp, its formation energy can be obtained using atomic chemical potentials μ_α as

$$\Delta H_{\mathrm{f}} = E_{\mathrm{T}}(\mathrm{defect};q) - E_{\mathrm{T}}(\mathrm{perfect}) + \sum_{\alpha} l_\alpha \mu_\alpha + q(E_{\mathrm{VBM}} + \varepsilon_{\mathrm{F}}), \tag{1}$$

where l_α is an integer. For instance, $l_\alpha=1$ indicates removal of the atom α from the perfect crystal into a reservoir, while

TABLE I. Calculated distances from vacancy sites to the surrounding atoms, together with coordinated atomic species and the coordination numbers. Since the HAp crystal has a low symmetry, atoms in a particular coordination shell centered at a vacancy site are not always located at the same distances. In such a case, averaged distances form the vacancy site are shown.

Site		Distance in nm (atomic species; coordination number)		
		1st NN	2nd NN	3rd NN
H^+	Bulk	0.098(O;1)	0.248(O;1)	0.271(Ca;3)
	Vacancy	0.154(O;1)	0.256(Ca;3)	0.262(O;1)
OH^-	Bulk	0.240(Ca;3)	0.320(O;6)	0.343(O;4)
		0.248(H;1)		
	Vacancy	0.255(H;1)	0.266(Ca;3)	0.285(O;2)
Ca-1^{2+}	Bulk	0.244(O;6)	0.264(O;1)	0.299(O;2)
	Vacancy	0.262(O;6)	0.284(O;1)	0.315(O;2)
Ca-$2a^{2+}$	Bulk	0.242(O;6)	0.271(H;1)	0.308(P;1)
			0.277(O;1)	
	Vacancy	0.153(H;1)	0.251(O;5)	0.271(O;1)
$(PO_4)^{3-}$-a	Bulk	0.308(Ca;1)	0.320(O;1)	0.330(Ca;1)
			0.321(Ca;1)	
	Vacancy	0.285(O;1)	0.334(O;1)	0.350(O;4)
				0.351(Ca;4)

$l_\alpha=-1$ corresponds to addition of α from a reservoir into the perfect crystal. In the present calculations, point defects arising from α=Ca, PO_4, OH, and H in their fully charged states (Ca^{2+}, PO_4^{3-}, OH^-, and H^+) are considered. It is then noted that the defect charge q is related to the ionic charge z_α for α as

$$q=-\sum_\alpha l_\alpha z_\alpha. \tag{2}$$

In Eq. (1), ε_F is the Fermi level measured from the valence band maximum (E_{VBM}). Since the E_{VBM} values for the defective supercells are affected by the supercell size and the background charges neutralizing the supercell charges, they are different from that of the perfect supercell. Therefore, E_{VBM} values of the defective supercells are corrected using average electrostatic potentials for atoms in the perfect and defective supercells ($V_{av}^{perfect}$ and V_{av}^{defect}) in the following manner:

$$E_{VBM}=E_{VBM}^{perfect}+V_{av}^{defect}-V_{av}^{perfect}=E_{VBM}^{perfect}+\Delta V_{av}. \tag{3}$$

More details for the ΔV_{av} evaluation were also described elsewhere.[17,26] Substituting Eqs. (2) and (3) into Eq. (1) gives the defect formation energy as

$$\Delta H_f=E_T(\text{defect};q)-E_T(\text{perfect})+\sum_\alpha l_\alpha(\mu_\alpha-z_\alpha E_{F,HAp})+q\Delta V_{av}. \tag{4}$$

Here the relation of $E_{F,HAp}=E_{VBM}^{perfect}+\varepsilon_F$ is used, which corresponds to the Fermi energy of the perfect supercell.

μ_α is generally determined from a particular chemical equilibrium condition. In fact, there were a number of theoretical calculations of defect formation energies assuming solid-solid or solid-gas equilibrium conditions.[27–29] Unlike the previous reports, the present study attempts to deal with solid-liquid equilibrium between solid HAp and the surrounding aqueous solution saturated with respect to HAp. Since the saturated solution is composed of ionic species such as Ca^{2+}, PO_4^{3-}, OH^-, and H^+, it is convenient to write Eq. (4) not by the atomic chemical potentials μ_α but by the chemical potentials for the charged species $\mu_{\alpha^{z_\alpha}}$. Note that the chemical potentials of ionic species α^{z_α} in HAp are obtained by $\mu_{\alpha^{z_\alpha}}=\mu_\alpha-z_\alpha E_{F,HAp}$, Eq. (4) can be expressed as

$$\Delta H_f=E_T(\text{defect};q)-E_T(\text{perfect})+\sum_\alpha l_\alpha\mu_{\alpha^{z_\alpha}}+q\Delta V_{av}. \tag{5}$$

In the chemical equilibrium between solid HAp and its saturated solution, the electrochemical potentials for a particular ionic species in the two phases ($\bar{\mu}_{\alpha^{z_\alpha},HAp}$ and $\bar{\mu}_{\alpha^{z_\alpha},aq}$) are equal to each other,[30,31]

$$\bar{\mu}_{\alpha^{z_\alpha},HAp}=\bar{\mu}_{\alpha^{z_\alpha},aq}. \tag{6}$$

In terms of inner potentials for HAp crystal ($\phi^{(HAp)}$) and its saturated solution ($\phi^{(aq)}$), the chemical potential $\mu_{\alpha^{z_\alpha},HAp}$ is given by

$$\mu_{\alpha^{z_\alpha},HAp}=\mu_{\alpha^{z_\alpha},aq}+z_\alpha(\phi^{(aq)}-\phi^{(HAp)})=\mu_{\alpha^{z_\alpha},aq}+z_\alpha\Delta_{HAp}^{aq}\phi. \tag{7}$$

The second term of the right-hand side in Eq. (7) is an electrostatic energy contribution for the charged species due to the inner-potential difference of $\Delta_{HAp}^{aq}\phi$. Combining Eqs. (5) and (7) provides the final form of the defect formation energy, as follows:

$$\Delta H_f = E_T(\text{defect};q) - E_T(\text{perfect}) + \sum_\alpha l_\alpha \mu_{\alpha^{z_\alpha},\text{aq}} + q\Delta V_{\text{av}} - q\Delta^{\text{aq}}_{\text{HAp}}\phi. \quad (8)$$

The inner-potential difference of the right-hand side in Eq. (8) cannot be evaluated straightforwardly, and may depend on concentrations of the defects. Hence this term is considered as a variable, and is used to calculate equilibrium defect concentrations of the charged point defects in HAp (shown in Sec. III C).

The chemical potential $\mu_{\alpha^{z_\alpha},\text{aq}}$ in Eq. (8) comprises a standard chemical potential term $\mu^\circ_{\alpha^{z_\alpha},\text{aq}}$ (at a temperature T and a pressure of 0.1 MPa) and a term of $k_B T \ln a_{\alpha^{z_\alpha}}$ as

$$\mu_{\alpha^{z_\alpha},\text{aq}} = \mu^\circ_{\alpha^{z_\alpha},\text{aq}} + k_B T \ln a_{\alpha^{z_\alpha}}, \quad (9)$$

where k_B is the Boltzmann constant and $a_{\alpha^{z_\alpha}}$ is an activity of ionic species α^{z_α} in the solution, which depends on the activity coefficient $\gamma_{\alpha^{z_\alpha}}$ and the concentration in the solution $[\alpha^{z_\alpha}]$ ($a_{\alpha^{z_\alpha}} = \gamma_{\alpha^{z_\alpha}}[\alpha^{z_\alpha}]$). For simplicity, activity coefficients for all species are approximated to be 1.0 throughout the present study. This would be reasonable in this case, since HAp is sparingly soluble in water[1] and its saturated solution is basically considered as dilute solution. Therefore, in order to evaluate the defect formation energy by using Eq. (8), the standard chemical potentials and concentrations of constituent ions in the aqueous solution, shown in Eq. (9), have to be prepared.

C. Standard chemical potentials of ionic species in aqueous solution

In order to calculate ΔH_f, it is necessary to obtain the standard chemical potential $\mu^\circ_{\alpha^{z_\alpha},\text{aq}}$ in Eq. (9). However, it is difficult to straightforwardly calculate this quantity in a first-principles manner. This is because ionic species in an aqueous solution are generally hydrated, and thus detailed atomic structures of hydrated ions should be correctly taken into account, which would be a very demanding task. To avoid this difficulty, experimental thermodynamic data are used in combination with total energies of reference solids and molecules from the first-principles calculations.

For example, in the case of Ca^{2+}, the quantity of $\mu^\circ_{Ca^{2+},\text{aq}}$ corresponds to a Gibbs energy change of the following reaction:

$$\text{Ca(s)} \rightarrow \text{Ca}^{2+}(\text{aq}, a_{\text{Ca}^{2+}} = 1) + 2\text{e}^-. \quad (10)$$

It should be noted that the Gibbs energy change for the independent Ca^{2+} ion in the aqueous solution cannot be measured experimentally. In conventional electrochemistry, the standard hydrogen electrode [SHE, $\text{Pt}|\text{H}_2(\text{g}, p = 0.1\ \text{MPa})|\text{H}^+(\text{aq}, a_{\text{H}^+}=1)$] is invoked, and the following reaction in the half cell of SHE:

$$\text{H}_2(\text{g}, p = 0.1\ \text{MPa}) \rightarrow 2\text{H}^+(\text{aq}, a_{\text{H}^+} = 1) + 2\text{e}^-, \quad (11)$$

is combined with the half cell of Eq. (10):

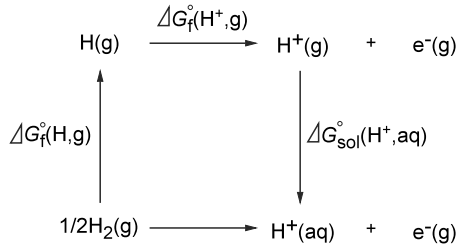

FIG. 2. Born-Harber cycle for formation of proton in aqueous solution.

$$\text{Ca(s)} + 2\text{H}^+(\text{aq}, a_{\text{H}^+} = 1) = \text{Ca}^{2+}(\text{aq}, a_{\text{Ca}^{2+}} = 1) + \text{H}_2(\text{g}, p = 0.1\ \text{MPa}). \quad (12)$$

The equilibrium condition for Eq. (12) can be written as

$$\mu^\circ_{\text{Ca,s}} + 2\bar{\mu}^\circ_{\text{H}^+,\text{aq}} = \bar{\mu}^\circ_{\text{Ca}^{2+},\text{aq}} + \mu^\circ_{\text{H}_2,\text{g}}. \quad (13)$$

It is noted that the standard electrochemical potentials are expressed in terms of standard chemical potentials and electrostatic potentials in the following manner:

$$\bar{\mu}^\circ_{\text{Ca}^{2+},\text{aq}} = \mu^\circ_{\text{Ca}^{2+},\text{aq}} + z_{\text{Ca}^{2+}}\phi^{\circ(\text{Ca,aq})},$$

$$\bar{\mu}^\circ_{\text{H}^+,\text{aq}} = \mu^\circ_{\text{H}^+,\text{aq}} + z_{\text{H}^+}\phi^{\circ(\text{SHE})}. \quad (14)$$

Then the standard Gibbs formation energy of Ca^{2+} in the aqueous solution $[\Delta G^\circ_f(\text{Ca}^{2+},\text{aq})]$ can be given by combination of Eqs. (13) and (14)

$$\Delta G^\circ_f(\text{Ca}^{2+},\text{aq}) = -2(\phi^{\circ(\text{Ca,aq})} - \phi^{\circ(\text{SHE})}) = \mu^\circ_{\text{Ca}^{2+},\text{aq}} + \mu^\circ_{\text{H}_2,\text{g}} - \mu^\circ_{\text{Ca,s}} - 2\mu^\circ_{\text{H}^+,\text{aq}}. \quad (15)$$

Standard Gibbs formation energies of various ions in an aqueous solution at 298 K are available in the thermodynamic table,[32] which are used in this study. Therefore, $\mu^\circ_{\text{Ca}^{2+},\text{aq}}$ can be rewritten from Eq. (15) as

$$\mu^\circ_{\text{Ca}^{2+},\text{aq}} = \Delta G^\circ_f(\text{Ca}^{2+},\text{aq}) + \mu^\circ_{\text{Ca,s}} + 2\left(\mu^\circ_{\text{H}^+,\text{aq}} - \frac{1}{2}\mu^\circ_{\text{H}_2,\text{g}}\right). \quad (16)$$

For the solid phase of pure Ca, bcc Ca is separately calculated from first principles, and the total energy per atom is considered to be equal to $\mu^\circ_{\text{Ca,s}}$.

In order to evaluate the third term in parentheses in Eq. (16), a Born-Haber-like cycle for hydrogen in Fig. 2 is invoked, and the following equation can be obtained:[31]

$$\mu^\circ_{\text{H}^+,\text{aq}} - \frac{1}{2}\mu^\circ_{\text{H}_2,\text{g}} = \Delta G^\circ_f(\text{H,g}) + \Delta G^\circ_f(\text{H}^+,\text{g}) + \Delta G^\circ_{\text{sol}}(\text{H}^+,\text{aq}) - \mu^\circ_{\text{e}^-,\text{g}}, \quad (17)$$

where $\Delta G^\circ_f(\text{H,g})$ is an atomization energy of a H_2 molecule, and $\Delta G^\circ_f(\text{H}^+,\text{g})$ is an ionization energy of a H atom. $\Delta G^\circ_{\text{sol}}(\text{H}^+,\text{aq})$ indicates a solvation energy of a proton in the solution of the SHE, and $\Delta G^\circ_{\text{sol}}(\text{H}^+,\text{aq}) = -11.28$ eV (at 298 K), provided that the aqueous solution of the SHE is

uncharged.[31] All these quantities at 298 K are tabulated in Ref. 31, which are used in this study. The last term of the right-hand side in Eq. (17) corresponds to a chemical potential of an ideal electron gas at the standard state, and the value of −0.04 eV at 298 K obtained from the Fermi-Dirac statistics is used for it.[33] As a result, the standard chemical potential for Ca^{2+} in the aqueous solution can be quantitatively evaluated.

For other ionic species relevant to HAp, their standard chemical potentials are represented in the similar way, and are summarized below

$$\mu^{\circ}_{PO_4^{3-},aq} = \Delta G^{\circ}_f(PO_4^{3-},aq) + \mu^{\circ}_{P,s} + 2\mu^{\circ}_{O_2,g} - 3\left(\mu^{\circ}_{H^+,aq} - \frac{1}{2}\mu^{\circ}_{H_2,g}\right), \tag{18}$$

$$\mu^{\circ}_{OH^-,aq} = \Delta G^{\circ}_f(OH^-,aq) + \frac{1}{2}(\mu^{\circ}_{O_2,g} + \mu^{\circ}_{H_2,g}) - \left(\mu^{\circ}_{H^+,aq} - \frac{1}{2}\mu^{\circ}_{H_2,g}\right). \tag{19}$$

The standard chemical potential for a proton in the solution can be easily obtained from Eq. (17). $\mu^{\circ}_{P,s}$ in Eq. (18) is a total energy per atom of solid black phosphorous (the *Acam* space group)[34,35] calculated in the first-principle manner.

In the above equations of Eqs. (16)–(19), the remaining terms to be prepared are the standard chemical potentials for the gas phases of O_2 and H_2. They are obtained from total energies of the isolated molecules, and it is also reasonable to take account of the temperature dependence of the chemical potentials.[17] For instance, $\mu^{\circ}_{H_2,g}$ is expressed in terms of the enthalpy $h^{\circ}_{H_2,g}(T)$ and entropy $S^{\circ}_{H_2,g}(T)$ as

$$\mu^{\circ}_{H_2,g} = h^{\circ}_{H_2,g}(T) - TS^{\circ}_{H_2,g}(T) = h^{\circ}_{H_2,g}(0) + [h^{\circ}_{H_2,g}(T) - h^{\circ}_{H_2,g}(0)] - TS^{\circ}_{H_2,g}(T). \tag{20}$$

A total energy for an isolated H_2 molecule by the first-principles calculations is considered to be the enthalpy at $T=0$ K $[h^{\circ}_{H_2,g}(0)]$, and the resultant temperature-dependent enthalpy and entropy terms are obtained from the thermodynamic data.[36] For evaluation of defect formation energies and defect concentrations, a temperature of 298 K is employed throughout the present study.

In order to assess the validity of the standard chemical potentials for ions shown above, the following dissociation equilibrium of HAp is examined:

$$Ca_5(PO_4)_3OH(s) = 5Ca^{2+}(aq) + 3PO_4^{3-}(aq) + OH^-(aq). \tag{21}$$

The equilibrium condition can be described by the ionic chemical potentials and the solubility product K_{sp} as

$$2.303k_BTpK_{sp} = 5\mu^{\circ}_{Ca^{2+},aq} + 3\mu^{\circ}_{PO_4^{3-},aq} + \mu^{\circ}_{OH^-,aq} - \mu^{\circ}_{HAp,s}, \tag{22}$$

where

$$pK_{sp} = -\log([Ca^{2+}]^5[PO_4^{3-}]^3[OH^-]). \tag{23}$$

From the total energy of perfect HAp $(=\mu^{\circ}_{HAp,s})$ and the standard chemical potentials of Eqs. (16), (18), and (19), the Gibbs energy change at the standard state in the right-hand side of Eq. (22) is calculated to be 325 kJ/mol. The calculated result is in good agreement with the experimental value of 328 kJ/mol, which is obtained from $2.303k_BTpK_{sp}$ in the left-hand side term of Eq. (22) using experimental $pK_{sp}=57.5$ in the molarity scale.[37]

D. Ionic concentrations in aqueous solution

Once the standard chemical potentials $\mu^{\circ}_{\alpha^{\xi}\alpha,aq}$ are given in the manner described above, the remaining quantity to be obtained in Eq. (9) is ionic concentrations in the aqueous solution. In equilibrium at $T=298$ K, concentrations of ionic species dissolving from HAp in the saturated aqueous solution are governed by the solubility product K_{sp}, as shown in Eq. (23). In this study, the experimental value of $pK_{sp}=57.5$ in the molarity scale[37] is used. From the ionic product of water $pK_w=14.0$ mol^2/l^2, the $[H^+]$ and $[OH^-]$ values are also constrained by

$$pK_w = -\log([H^+][OH^-]). \tag{24}$$

It should be noted here that phosphate ions in the HAp-saturated aqueous solution can be present in three different protonated forms such as HPO_4^{2-}, $H_2PO_4^-$, and H_3PO_4, depending on pH $(=-\log[H^+])$ of the aqueous system. Their concentrations are determined by the following acid dissociation constants in the molarity scale:

$$pK_1 = -\log(([PO_4^{3-}][H^+])/[HPO_4^{2-}]) = 12.3, \tag{25}$$

$$pK_2 = -\log(([HPO_4^{2-}][H^+])/[H_2PO_4^-]) = 7.2, \tag{26}$$

$$pK_3 = -\log(([H_2PO_4^-][H^+])/[H_3PO_4]) = 2.1. \tag{27}$$

Moreover, charge neutrality of the solution has to be taken into account. In this regard, it is assumed that acid HX (in the low pH range) or base MOH (in the high pH range) is added to adjust the pH value, where M^+ and X^- are indifferent ions to the dissolution equilibrium of HAp.[37] For instance, in the low pH range, the ionic concentrations are constrained as

$$2[Ca^{2+}] + [H^+] = [X^-] + [OH^-] + 3[PO_4^{3-}] + 2[HPO_4^{2-}] + [H_2PO_4^-], \tag{28}$$

where

$$[H^+] = [X^-]. \tag{29}$$

Similarly, in the high pH range, the charge-neutrality requirement can be expressed by

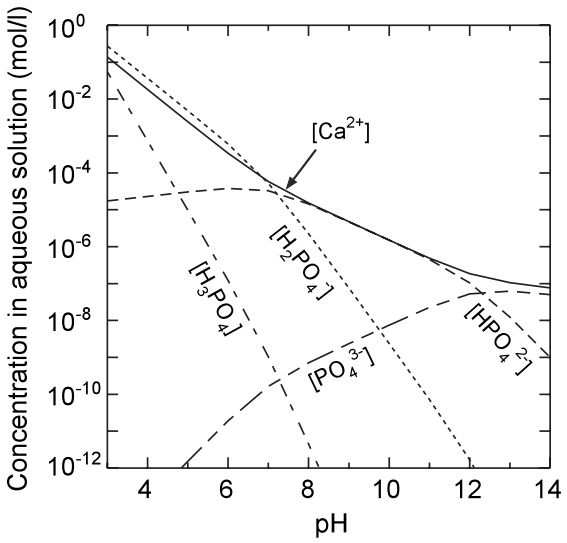

FIG. 3. pH dependence of concentrations of ionic species in the aqueous solution saturated with HAp.

$$2[\mathrm{Ca}^{2+}] + [\mathrm{H}^{+}] + [\mathrm{M}^{+}] = [\mathrm{OH}^{-}] + 3[\mathrm{PO}_4^{3-}] + 2[\mathrm{HPO}_4^{2-}] + [\mathrm{H}_2\mathrm{PO}_4^{-}], \quad (30)$$

where

$$[\mathrm{M}^{+}] = [\mathrm{OH}^{-}]. \quad (31)$$

A pH value is considered as a variable parameter, and ion concentrations in the HAp-saturated solution at a particular pH can be calculated from Eqs. (23)–(31), which are used to evaluate the ionic chemical potentials in Eq. (9) and their pH dependence.

Figure 3 shows the calculated pH dependence of ionic concentrations in the HAp-saturated solution. The calcium concentration decreases with increasing pH, and the $[\mathrm{Ca}^{2+}]$ profile is in agreement with the result by Chander and Fuerstenau.[38] Among phosphate-related ions, the HPO_4^{2-} and $\mathrm{H}_2\mathrm{PO}_4^{-}$ dominate in the solution around neutral pH, and the amount of PO_4^{3-} is quite small expect for in the extremely high pH range. It can be said that phosphate ions dissolving from HAp easily accept protons in the solution, and most of them are in the protonated form such as HPO_4^{2-} and $\mathrm{H}_2\mathrm{PO}_4^{-}$.

III. RESULTS AND DISCUSSION

A. Electronic structures of vacancies in HAp

Figure 4 shows calculated densities of states (DOSs) for supercells with and without an isolated vacancy in HAp. For the defective supercells, energy positions of the valence band maximum (VBM) are corrected by the average potentials, which are set at 0 eV. In this figure, only the DOS curves for five kinds of vacancies at particular atomic sites are displayed, because DOS profiles for vacancies located at other inequivalent atomic positions exhibit quite similar features to those shown here. In addition, distances from the vacancies to neighboring atoms are summarized in Table I, together with the corresponding interatomic distances in the perfect lattice.

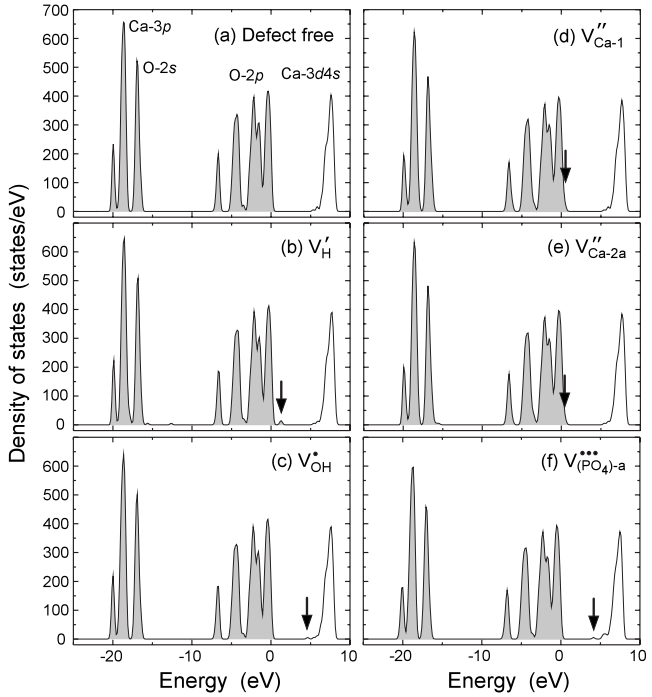

FIG. 4. Calculated densities of states for the defect-free and the defective supercells involving intrinsic vacancies. The notation of $V^{\bullet\bullet\bullet}_{(PO_4)-a}$ in (f) indicates a charged vacancy of PO_4^{3-} centered at the P-a site. The VBM for each supercell is set at 0 eV. Shaded areas indicate electron-occupied bands.

The valence band (VB) structure of hexagonal HAp was already discussed in detail elsewhere,[10,11,17] which is readily applicable to the monoclinic case. This can be easily imagined because a main structural difference between the hexagonal and monoclinic phase is arrangement of OH groups along the *c* axis (see also Fig. 1).[1,23] The lower VB around −20 eV comprises Ca-3*p* and O-2*s* orbitals, and the upper VB consists of O-2*p* components. The conduction band (CB) above the band gap is mainly composed of Ca-3*d*4*s* orbitals. The theoretical band gap of defect-free *m*-HAp is 5.3 eV, which is almost the same with that for the hexagonal case.[10,11,17]

In the presence of the vacancies, extra energy levels indicated by the arrows appear around the band gap. Although contour plots of the extra wave functions are not explicitly shown here, except for the case of $V^{\bullet\bullet\bullet}_{(PO_4)-a}$ (shown later in Fig. 6), it is confirmed that the wave functions are mainly composed of orbital components of atoms neighboring the vacancies, and their localized features around V'_H, $V^{\bullet}_{OH}$, $V''_{Ca\text{-}1}$, and $V''_{Ca\text{-}2a}$ are almost the same with the results in Fig. 5 of Ref. 17. The extra level for V'_H located above the VBM has considerable 2*p* components of oxygen at the first nearest neighboring (1st NN) site (0.154 nm in distance, see Table I) that was in the same OH^- group before formation of the H^+ vacancy. It can be thus said that this wave function is an acceptorlike one coming from the VB. On the other hand, the $V^{\bullet}_{OH}$ defect exhibits the extra level below the conduction band minimum (CBM). It is found that the extra level is mainly composed of Ca-3*d*4*s* orbitals at the 2nd NN sites

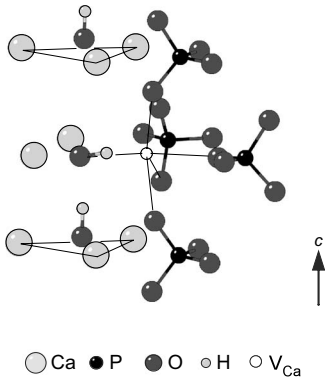

FIG. 5. Optimized atomic structure around $V''_{Ca\text{-}2a}$. The open circle at the center indicates the original Ca-2a position that is removed to form the vacancy. Thin lines represent the triangles formed by Ca-2 ions around the OH^- columns and the oxygen ions in the second coordination shell from the Ca-2a vacancy site (see Table I).

(Table I), and thus is a donorlike one coming from the CB.

Similar to V'_H, the $V''_{Ca\text{-}1}$ and $V''_{Ca\text{-}2a}$ defects have shallow acceptorlike levels just above the VBM. The wave functions consist mainly of O-2*p* orbitals at the 1st NN sites for $V''_{Ca\text{-}1}$ and at the 2nd NN sites for $V''_{Ca\text{-}2a}$ (Table I). It is noted that, in the case of $V''_{Ca\text{-}2a}$, a hydrogen is the 1st NN atom from $V''_{Ca\text{-}2a}$ (0.153 nm in distance). As can be seen in the atomic structure around $V''_{Ca\text{-}2a}$ (Fig. 5), the OH^- group adjacent to the vacancy is rotated off from the *c*-axis direction, maintaining the same O-H distance with that in bulk (0.098 nm). This is due to electrostatic interactions between OH^- and $V''_{Ca\text{-}2a}$, where the positively charged H and negatively charged O atoms in the OH group are oriented toward and away from negatively charged $V''_{Ca\text{-}2a}$, respectively. Such a characteristic atomic structure is also found for $V''_{Ca\text{-}2b}$ and $V''_{Ca\text{-}2c}$, because three kinds of the Ca-2 sites are located close to the OH columns along the *c* axis, unlike the Ca-1 and Ca′-1 sites (see Fig. 1).

Regarding $V^{\bullet\bullet\bullet}_{(PO_4)\text{-}a}$, which denotes a vacancy of PO_4^{3-} centered at a P-a atom, its DOS profile of Fig. 4(f) exhibits an extra level below the CBM. From the contour map of the wave function (Fig. 6), this level is localized at the vacancy site, and its main component is Ca-3*d*4*s* orbitals, which is similar to the case of $V^{\bullet}_{OH}$. In the relaxed structure (see Table I), the 1st and 2nd NN Ca atoms from the vacancy site in the unrelaxed state tend to move away from the vacancy, due to electrostatic repulsion of $V^{\bullet\bullet\bullet}_{(PO_4)\text{-}a}$ and Ca^{2+}, whereas the surrounding negatively charged O atoms tend to come close to the vacancy by attractive electrostatic interactions with $V^{\bullet\bullet\bullet}_{(PO_4)\text{-}a}$. As a result, the Ca atoms contributing the defect-induced wave function are no longer 1st NN atoms for the vacancy, but are located at the 3rd NN sites (0.351 nm in distance).

B. Interstitial and substitutional protons in HAp

In this subsection, electronic and atomic structures of protons located at interstitial sites and at Ca sites are investi-

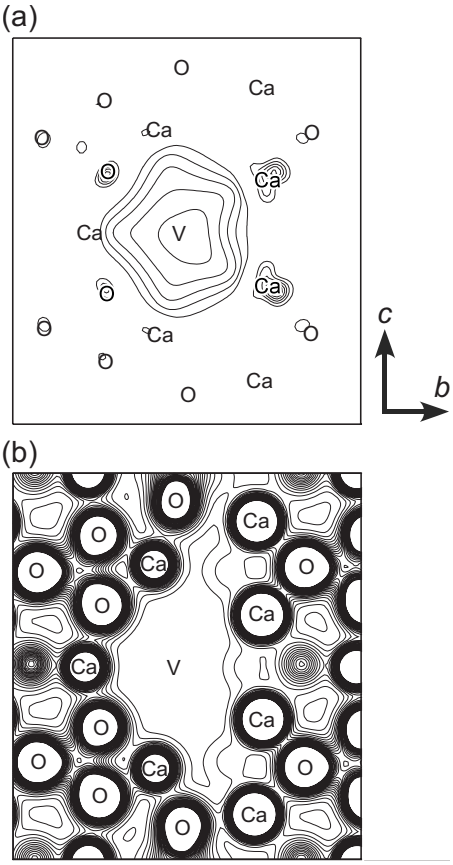

FIG. 6. Contour maps of (a) the defect-induced wave function and (b) the valence-electron density for $V^{\bullet\bullet\bullet}_{(PO_4)-a}$. The PO_4^{3-} vacancy position is represented by "V."

gated. In HAp, it is expected that interstitial protons are stable by attaching to oxygen ions of OH^- or PO_4^{3-} groups, namely, forming H_2O^0 or HPO_4^{2-}.[39] In this study, therefore, five kinds of interstitial positions for protons, shown in Fig. 7, are considered. These interstitial positions are located around OH^- and the PO_4^{3-} centered at the P-b atom and the following three items are taken into account for generating initial structures for the interstitial protons: (1) An interstitial proton is put around oxygen with 0.1 nm in distance, (2) the proton of the O-H bond then generated points to the nearest neighboring oxygen atom at the vertex of an adjacent PO_4^{3-}, and (3) is located as far away from the neighboring Ca atoms as possible. As a result, the $H^{\bullet}_{i\text{-}1}$ defect corresponds to interstitial H^+ attaching to the OH group, and other four interstitials (from $H^{\bullet}_{i\text{-}2}$ to $H^{\bullet}_{i\text{-}5}$) are situated between oxygen atoms of adjacent PO_4^{3-} groups. On the other hand, as substitutional defects, protons at five inequivalent Ca sites (see Fig. 1) with an effective charge of −1, are calculated (for instance, denoted by $H'_{Ca\text{-}1}$ for the proton at the Ca-1 site).

As a typical example, total and atom-projected partial DOS curves for $H^{\bullet}_{i\text{-}1}$ and $H'_{Ca\text{-}1}$ are shown in Fig. 8. Extra peaks having considerable H-1*s* components can be observed around −9 ~ −8 eV in the total and partial DOS curves (the arrows in the figure). Figure 9 shows the contour map of the wave function at −8.3 eV for $H^{\bullet}_{i\text{-}1}$, together with the optimized atomic structure. It is found that the $H^{\bullet}_{i\text{-}1}$ defect around

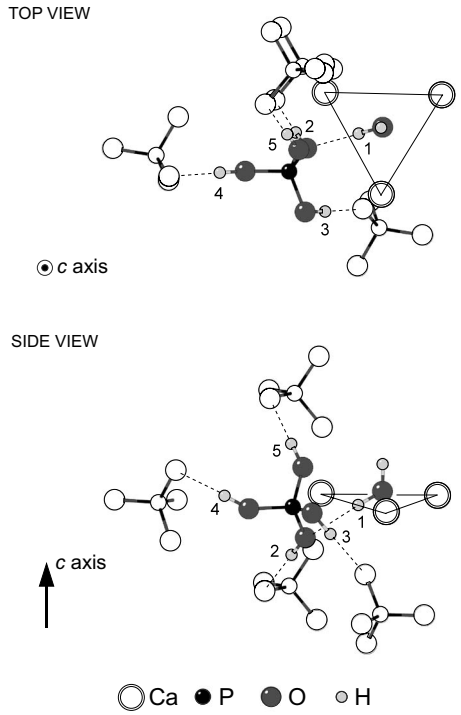

FIG. 7. Illustrations representing initial atomic positions for interstitial protons in HAp. In the present study, five kinds of different interstitial sites are considered, which are numbered in this figure. For clarity, only the PO_4^{3-} tetrahedron and OH^- group attached by the interstitials are highlighted, and the surrounding ions and groups are drawn by open circles, irrespective of atomic species. Triangles drawn by thin solid lines around the OH^- group indicate the ones formed by the triangular Ca-2 ions.

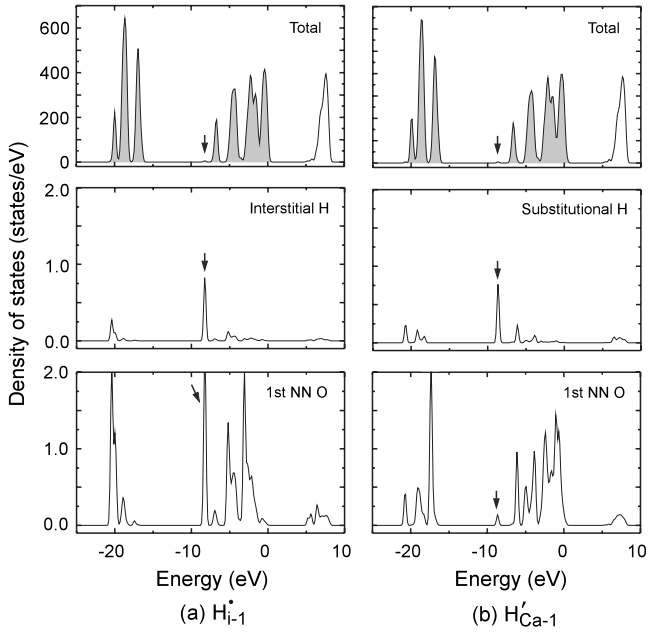

FIG. 8. Total and partial DOS curves for HAp supercells containing $H^{\bullet}_{i-1}$ and H'_{Ca-1}. The VBM values are set at 0 eV. Shaded areas in the total DOSs indicate electron-occupied bands.

the OH^- group forms the H_2O^0 group, and the wave function corresponds to bonding between H-O in the H_2O^0 group. In fact, the partial DOS for O directly bonded to $H^{\bullet}_{i-1}$ [the bottom figure of Fig. 8(a)] also shows the strong peak at the same energy position. It is noted that the H-O length and ∠H-O-H angle in the H_2O^0 group is about 0.10 nm and 107.8°, and the angle is slightly larger than that of an isolated H_2O molecule (104.5°).

Likewise, the extra level appearing at −8.7 eV for H'_{Ca-1} [Fig. 8(b)] arises from 1*s* components of the substituting proton for Ca-1. However, the local atomic structure of the proton is quite different from that of $H^{\bullet}_{i-1}$. Figure 10(a) displays the optimized atomic structure around H'_{Ca-1}. The Ca-1 site is originally surrounded by six O atoms at vertices of different PO_4^{3-} tetrahedra (also see Table I). After optimization, the proton is no longer located at the Ca-1 site, but attaches to one of the neighboring O atoms with an H-O length of 0.10 nm, where the H^+ defect is situated 0.13 nm away from the Ca-1 site. In other words, the acid phosphate (HPO_4^{2-}) is formed adjacent to the Ca-1 vacancy. The extra peak at −8.7 eV in the partial DOS of the introduced proton corresponds to a bonding wave function for the H-O bond of the HPO_4^{2-} group. Such a characteristic local structure is also found for $H'_{Ca'-1}$.

In Figs. 10(b) and 10(c), calculated atomic arrangements around H'_{Ca-2a}, and $H^{\bullet}_{i-2}$ are displayed. Unlike the case of H'_{Ca-1}, the proton in H'_{Ca-2a} does not have bonding to an O atom of surrounding PO_4^{3-} groups, but considerably moves toward the OH^- group to form H_2O^0 [Fig. 10(b)], in the similar way to $H^{\bullet}_{i-1}$. Simultaneously, it turns out that the H_2O^0 group is rotated so as to make the two H-O bonds pointing to O atoms of the adjacent PO_4^{3-} groups, which suggests tendency of hydrogen-bonding interactions of O-H···O. It is most likely, therefore, that the H'_{Ca-2a} defect is stabilized by formation of the H_2O^0 group and the resultant hydrogen bonding. The interstitial proton $H^{\bullet}_{i-2}$ [Fig. 10(c)] also forms the O-H bond, and is located between two oxygen ions belonging to different PO_4^{3-} groups.

As is well known, hydrogen bonding plays a major role for cohesion of H_2O molecules in ice and water. Pálinkás *et al.* defined the presence of hydrogen bonds between two H_2O molecules from the O···O distance of the two molecules of less than 0.328 nm and the angle between the O-H bond vector and the O···O vector (∠H-O···O) of less than 20°.[40] According to this definition, the local atomic structures of the interstitial and substitutional protons in HAp are analyzed, from the geometrical viewpoint related to hydrogen bonding. Table II shows O-H^* bond lengths, O···O distances, and ∠H^*-O···O angles around the interstitial and substitutional protons that are denoted by H^* in this table. It can be seen that the local bonding configurations of $H^{\bullet}_i$ and H'_{Ca-2} defects satisfy the above definition, so that they are considered to make hydrogen bonding with the surrounding PO_4^{3-} groups [see also Figs. 9(a) and 10(b)]. In fact, the O···O distances for $H^{\bullet}_i$ and H'_{Ca-2} (about 0.26 nm) are much smaller than those in the perfect HAp lattice (about 0.30 nm for two neighboring PO_4^{3-} and about 0.33 nm for the OH^- and its adjacent PO_4^{3-} group), which further indicates hydrogen-bonding formation due to the proton incorporation. Additionally, it is noted that the H'_{Ca-2} defects form H_2O^0

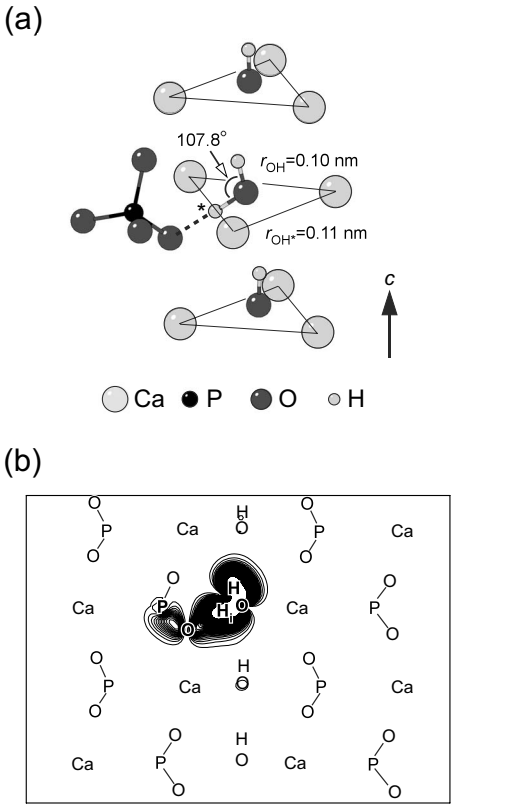

FIG. 9. Optimized atomic structure of $H_{i\text{-}1}^{\bullet}$ in HAp (a), and the contour map of the defect-induced wave function (b). The thick broken line connecting the interstitial proton and the oxygen atom in (a) indicates hydrogen bonding between the atoms. In (b), only atomic positions close to the cross sectional plane are depicted.

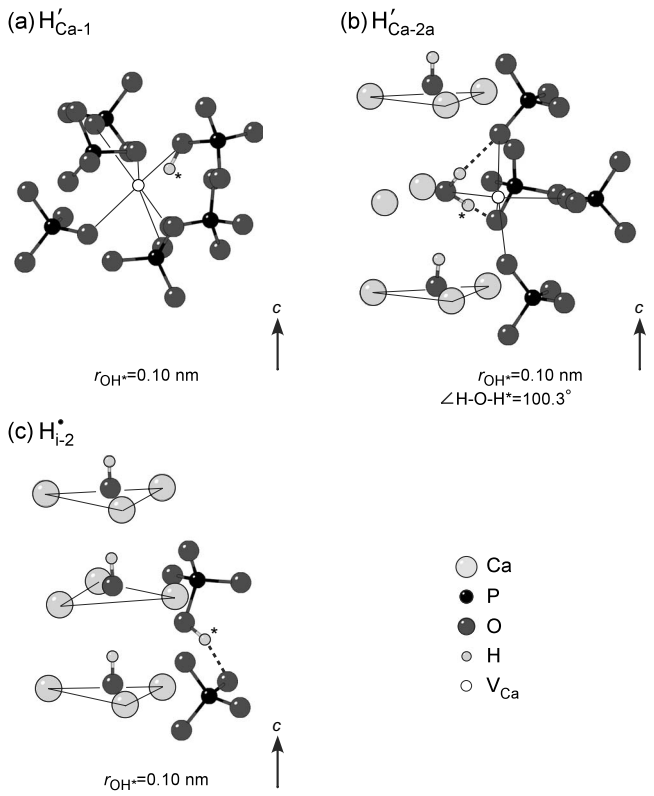

FIG. 10. Optimized atomic structures around $H'_{Ca\text{-}1}$, $H'_{Ca\text{-}2a}$, and $H_{i\text{-}2}^{\bullet}$. Protons introduced as defects are indicated by asterisks. Open circles in (a) and (b) represent initial atomic sites of protons substituting for the Ca ions, and the nearest neighboring oxygen ions from the vacancy sites are depicted by thin solid lines. In (b) and (c), the triangles by Ca-2 ions are also drawn. Thick broken lines suggest hydrogen bonding between OH and its neighboring O.

groups by being bonded to OH^-, and that another O-H bonds in the H_2O^0 groups are also hydrogen bonded to adjacent PO_4^{3-} groups (see the values in parentheses in Table II). This situation can be observed in Fig. 10(b), which will favor formation of the substitutional protons.

In contrast, the $H'_{Ca\text{-}1}$ and $H'_{Ca'\text{-}1}$ defects [Fig. 10(a)] have larger $\angle H^*\text{-}O\cdots O$ angles than the angle criterion of 20° for hydrogen bonding formation. It can be considered, therefore, that the protons no longer have hydrogen bonding interactions with the surrounding PO_4^{3-} groups, unlike $H_i^{\bullet}$ and $H'_{Ca\text{-}2}$. In fact, the $O\cdots O$ distances in $H'_{Ca\text{-}1}$ and $H'_{Ca'\text{-}1}$ are also larger, indicating their weak hydrogen bonding interactions with the neighboring PO_4^{3-} groups.

C. Formation energies and equilibrium concentrations of defects

From total energies of supercells containing the individual defect species, their formation energies and equilibrium concentrations in HAp are calculated. For a point defect β with a formation energy of ΔH_f, its equilibrium concentration C_β can be obtained as follows:

$$C_\beta = N_\beta \exp(-\Delta H_f / k_B T). \tag{32}$$

Here, N_β is the number of sites per unit volume for the defect. In the present case, N_β is 3.7×10^{21} cm^{-3} for defects at Ca^{2+}, PO_4^{3-}, and OH^- sites, while 1.1×10^{22} cm^{-3} for interstitial protons at the sites 2 to 5 (see Fig. 7). In this formula, interactions between defects are not taken into account explicitly. Due to charge neutrality requirement in the HAp crystal, the concentrations of isolated point defects with effective charge q_β are constrained as

$$\sum_\beta q_\beta C_\beta - n + p = 0, \tag{33}$$

where n and p represent electron and hole concentrations at VB and CB edges, respectively. However, it is assumed here to be $n=p=0$ because HAp is essentially considered to be an insulator with the large theoretical band gap of 5.3 eV. As stated earlier, the inner potential term $\Delta_{HAp}^{aq}\phi$ in Eq. (8) is used as a variable to determine the charged-defect concentrations from Eq. (33).

Figure 11 shows variations of ΔH_f for the charged defect species as a function of pH. Except for $V_H^{\bullet}$ and $V_{OH}^{\bullet}$, defect formation energies at possible inequivalent atomic sites in the HAp lattice are calculated (see Secs. III A and II B), but only the results showing the lowest formation energies for the respective defect species are displayed here. It is obvious that $H'_{Ca\text{-}2a}$ and $H_{i\text{-}1}^{\bullet}$ exhibit smaller formation energies over the entire pH range, as compared to other defects, and their

TABLE II. Interatomic distances and bond angles around interstitial and substitutional protons. Here, protons introduced as the defects are denoted by H^* in this table, in order to distinguish them from protons in the lattice OH^- groups. The O···O distances are the ones between two oxygen atoms neighboring to H^* that would be considered as hydrogen bonding linkages. In the cases of substitutional protons at the Ca-2 sites, values in parentheses indicate results for protons of the lattice OH^- groups that form H_2O^0 groups with the substitutional protons [see Fig. 10(b)].

Defect	O-H^* length (nm)	O···O distance (nm)	$\angle H^*$-O···O (deg.)
$H^{\bullet}_{i\text{-}1}$	0.105	0.257	2.4
$H^{\bullet}_{i\text{-}2}$	0.101	0.267	14.1
$H^{\bullet}_{i\text{-}3}$	0.106	0.251	5.7
$H^{\bullet}_{i\text{-}4}$	0.106	0.255	6.8
$H^{\bullet}_{i\text{-}5}$	0.101	0.269	18.0
$H'_{Ca\text{-}1}$	0.099	0.328	28.7
$H'_{Ca'\text{-}1}$	0.099	0.320	23.4
$H'_{Ca\text{-}2a}$	0.103 (0.099)	0.259 (0.323)	11.7 (7.0)
$H'_{Ca\text{-}2b}$	0.101 (0.099)	0.266 (0.303)	14.0 (3.3)
$H'_{Ca\text{-}2c}$	0.103 (0.099)	0.260 (0.323)	12.1 (6.9)

formation energies decrease with decreasing pH. Since the lower pH value indicates larger H^+ concentrations in the aqueous solution equilibrating with HAp, it is understood that the proton-related defects are easily introduced in HAp.

Figure 12(a) displays pH dependence of total equilibrium concentrations for the individual defect species at 298 K. As can be imagined from Fig. 11, the $H^{\bullet}_i$ and H'_{Ca} defects can be formed more abundantly than the other defect species. Since a number of possible defect locations are considered for $H^{\bullet}_i$ and H'_{Ca} (e.g., see Fig. 7), the concentrations at the different defect sites are separately plotted in Figs. 12(b) and 12(c). In the case of the interstitials [Fig. 12(b)], the concentration of

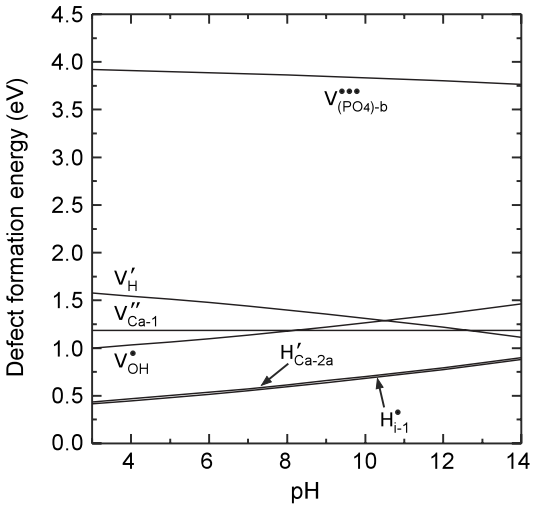

FIG. 11. Changes in the defect formation energies in HAp as a function of pH. In this plot, interactions between charged defect species are not taken into account. For each defect species, only the result for the most stable defect site is shown.

$H^{\bullet}_{i\text{-}1}$ is by several orders of magnitudes larger than those of the other interstitials, which corresponds to a formation energy difference of more than 0.16 eV. The $H^{\bullet}_{i\text{-}1}$ defect forms a H_2O^0 group by attaching to the lattice OH^- group, while the other interstitials are in the form of HPO_4^{2-} [see Figs. 9 and 10(c)]. The H_2O^0-group formation results in the smaller formation energy of $H^{\bullet}_{i\text{-}1}$. On the other hand, substitutional protons at Ca-2 sites have much larger concentrations, as compared to protons at Ca-1 sites [Fig. 12(c)]. In fact, it is found that ΔH_f values for the $H'_{Ca\text{-}2}$ defects are by more than 0.18 eV smaller than those for $H'_{Ca\text{-}1}$. Such a difference in formation energy can also be attributed to formation of the H_2O^0 group and the resultant hydrogen bonds with the adjacent PO_4^{3-} groups [see Figs. 10(a) and 10(b), and Table II].

From the results shown above, it seems likely that $H^{\bullet}_{i\text{-}1}$ and $H'_{Ca\text{-}2}$ are dominant in HAp in equilibrium with the HAp-satulated aqueous solution. However, when the numbers of sites for the defect species in the original HAp lattice are considered ($N_\alpha \approx 10^{21} \sim 10^{22}$ cm^{-3}), their calculated defect concentrations are still too small to conclude that the defects are responsible for the nonstoichiometry of HAp. Accordingly, effects of defect association are further investigated. Defect association often reduces defect formation energies due to electrostatic interactions between charged point defects. In particular, the above two defects of $H^{\bullet}_{i\text{-}1}$ and $H'_{Ca\text{-}2}$, whose formation is energetically more favorable among the charged species, are located around the lattice OH^- groups along the c axis, so that their association is spatially possible. Then a charge-neutral defect complex of $(H'_{Ca\text{-}2c}, H^{\bullet}_{i\text{-}1})^{\times}$ is calculated here. In this case, the 352-atom supercells are also used, where the respective defect species in the complexes are put in their nearest neighboring configuration. In addition to them, for comparison, defect complexes of $(H'_{Ca\text{-}2c}, V^{\bullet}_{OH})^{\times}$, $(V''_{Ca\text{-}1}, 2H^{\bullet}_i)^{\times}$, $(V'_H, V^{\bullet}_{OH})^{\times}$, and $(V''_{Ca\text{-}2c}, 2V^{\bullet}_{OH})^{\times}$ are also calculated in the aforementioned manner.

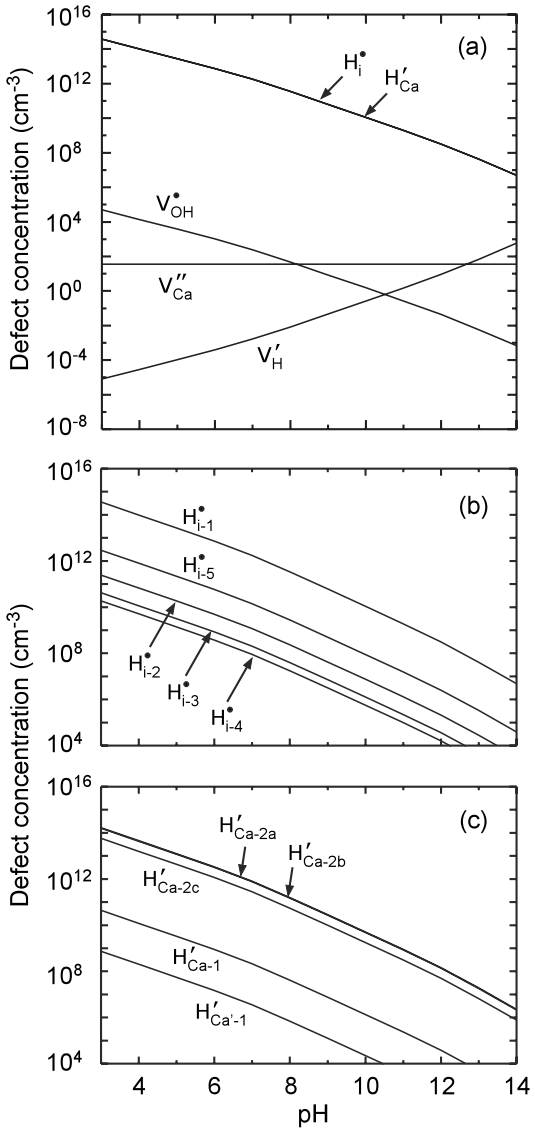

FIG. 12. Equilibrium defect concentrations in HAp against pH. (a) total concentrations of respective defect species, (b) concentrations of interstitial protons at different sites, and (c) those of protons at different substitutional Ca sites.

Figure 13 shows the formation energies and concentrations (at 298 K) of the defect complexes as a function of pH. In Fig. 13(b), only the concentration profiles for $(H'_{Ca\text{-}2c},H^{\bullet}_{i\text{-}1})^{\times}$ and $(V''_{Ca\text{-}1},2H^{\bullet}_{i})^{\times}$ can be observed, because concentrations of the other defect complexes are much smaller than the two defect complexes. It is obvious that the defect complexes tend to have smaller formation energies, as compared to the isolated charged defects as shown in Fig. 11, indicating the pronounced effect of defect association. It is worth mentioning here that the $(H'_{Ca\text{-}2c},H^{\bullet}_{i\text{-}1})^{\times}$ complex is most stable and its formation energy decreases with lowering pH to become zero around pH=5.5. Therefore, its concentration increases with decreasing pH and saturates below pH of around 5.5. This suggests that Ca-2c ions are completely replaced by protons in such a low pH range.

The $(V''_{Ca\text{-}1},2H^{\bullet}_{i})^{\times}$ defect complex also shows a smaller formation energy than $(H'_{Ca\text{-}2c},V^{\bullet}_{OH})^{\times}$, $(V''_{Ca\text{-}2c},2V^{\bullet}_{OH})^{\times}$, and

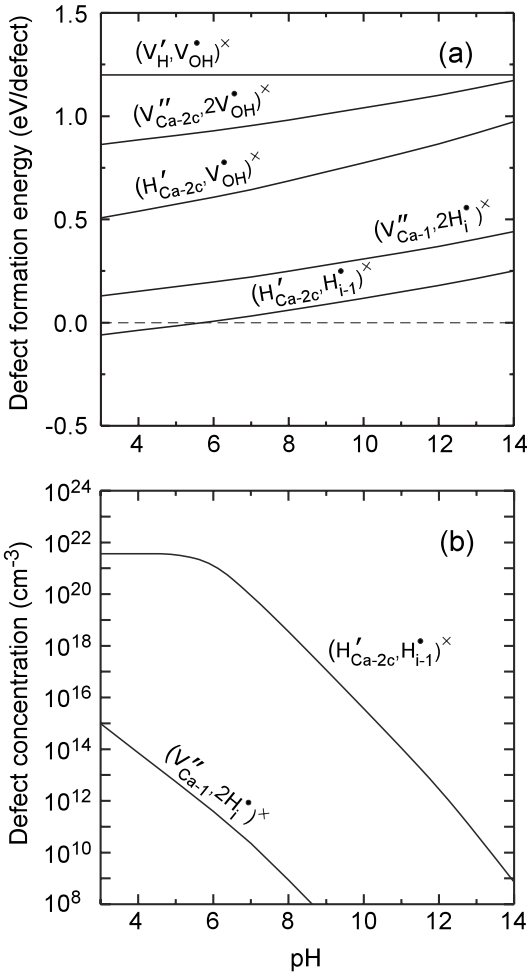

FIG. 13. Calculated formation energies and equilibrium concentrations of defect complexes as a function of pH.

$(V'_H,V^{\bullet}_{OH})^{\times}$, whereas its formation energy is more than 0.2 eV larger than $(H'_{Ca\text{-}2c},H^{\bullet}_{i\text{-}1})^{\times}$. This results in that the concentration of $(V''_{Ca\text{-}1},2H^{\bullet}_{i})^{\times}$ becomes by many orders of magnitude smaller in the entire pH range, as compared with that of $(H'_{Ca\text{-}2c},H^{\bullet}_{i\text{-}1})^{\times}$.

Figure 14 depicts the optimized atomic structures of $(H'_{Ca\text{-}2c},H^{\bullet}_{i\text{-}1})^{\times}$, $(V''_{Ca\text{-}1},2H^{\bullet}_{i})^{\times}$, and $(H'_{Ca\text{-}2c},V^{\bullet}_{OH})^{\times}$. In the $(H'_{Ca\text{-}2c},H^{\bullet}_{i\text{-}1})^{\times}$ complex [Fig. 14(a)], the H^+ defect substituting for Ca-2c is no longer located at the original position but moves into the neighboring O atom to form HPO_4^{2-}, making a hydrogen-bonding linkage of O-H$\cdots$O with the neighboring PO_4^{3-} group. The $H^{\bullet}_{i\text{-}1}$ defect in this complex still stays next to the OH^- group, and the H_2O^0 group then formed is rotated to make two hydrogen-bonding linkages with the two adjacent PO_4^{3-} groups. In Table III, the presence of hydrogen bonding in $(H'_{Ca\text{-}2c},H^{\bullet}_{i\text{-}1})^{\times}$ can be understood from the O$\cdots$O distances and the $\angle H^{*}$-O$\cdots$O angles satisfying the geometrical criterions for hydrogen bonding by Pálinkás *et al.*[40] Such formation of hydrogen-bonding linkages around the Ca-2c site may contribute to the stability of the defect complex.

On the other hand, the atomic structure of the $(V''_{Ca\text{-}1},2H^{\bullet}_{i})^{\times}$ complex [Fig. 14(b)] also resembles that of the

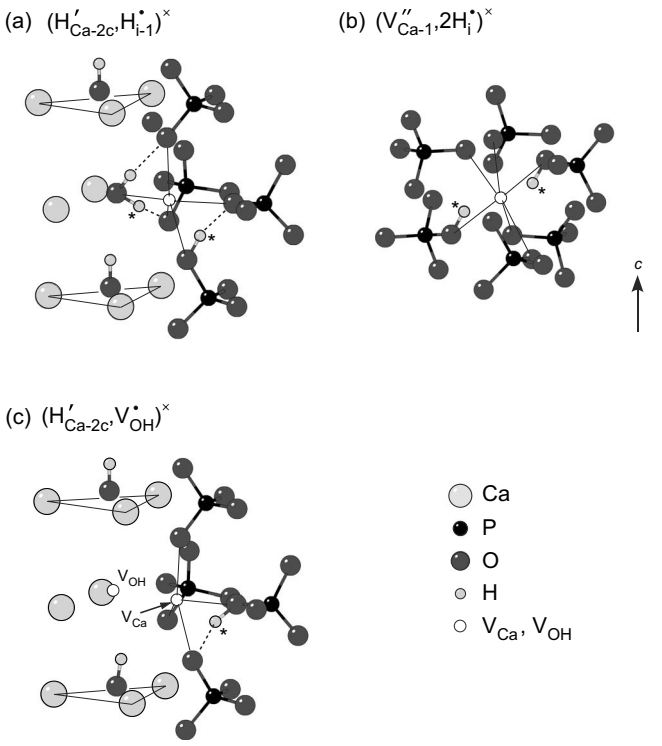

FIG. 14. Optimized atomic structures of defect complexes $(H'_{Ca\text{-}2c},H^{\bullet}_{i\text{-}1})^{\times}$, $(V''_{Ca\text{-}1},2H^{\bullet}_{i})^{\times}$, and $(H'_{Ca\text{-}2},V^{\bullet}_{OH})^{\times}$. These are drawn in the same manner with Fig. 10.

$H'_{Ca\text{-}1}$ defect shown in Fig. 10(a). The two interstitial protons have bonding with O atoms at the 1st NN sites from the Ca-1 site (O-H bond length of 0.10 nm). However, the two O-H bond directions are tilted by 22.8° and 24.9° toward the $V''_{Ca\text{-}1}$ site from the O···O lines of the neighboring PO_4^{3-} groups (Table III). This indicates that the hydrogen bonding is rather weak and alternatively the protons are attracted toward the vacancy site due to electrostatic interactions between H^+ and $V''_{Ca\text{-}1}$. In the case of $(H'_{Ca\text{-}2c},V^{\bullet}_{OH})^{\times}$, the proton originally located at the Ca-2c site attaches to the PO_4^{3-} group and tends to form the O-H^*···O linkage with the adjacent PO_4^{3-} group.

As stated earlier, a number of models for point defects in Ca-deficient HAp were proposed, where introduction of protons to the HAp lattice is responsible for the Ca deficiency.[2–9] In this regard, the present calculations show that the proton-related defects exhibit much smaller formation energies than other defects irrelevant to protons, and the $(H'_{Ca\text{-}2},H^{\bullet}_{i\text{-}1})^{\times}$ defect is abundantly formed in the low pH range. As shown in the optimized structure of $(H'_{Ca\text{-}2c},H^{\bullet}_{i\text{-}1})^{\times}$ in Fig. 14(a), the proton originally substituting for the Ca-2c ion is no longer situated at that site, and forms HPO_4^{2-} by being hydrogen-bonded to the adjacent PO_4^{3-} group. As a result, the defect structure of $(H'_{Ca\text{-}2c},H^{\bullet}_{i\text{-}1})^{\times}$ can also be regarded as the associated defect complex of $(V''_{Ca\text{-}2},2H^{\bullet}_{i})^{\times}$, which is close to the mechanism by Posner *et al.*[2–4] In the present case, however, one proton charge-compensating for Ca^{2+}vacancies is in the form of H_2O^0 by being bonded to the lattice OH^- groups. It should be noted that the formation of $(V''_{Ca\text{-}1},2H^{\bullet}_{i})^{\times}$ is also the similar charge-compensation mechanism but its concentration is found to be quite small [Fig. 13(b)]. The Ca vacancy formation due to proton incorporation strongly depends on the atomic sites in the HAp crystal structure.

As shown in Fig. 14(c), the substitutional proton in the $(H'_{Ca\text{-}2c},V^{\bullet}_{OH})^{\times}$ also undergoes significant displacements from the Ca-2c site to the interstitial site to form HPO_4^{2-}, so that the defect configuration can be described in a different way as $(V''_{Ca\text{-}2c},V^{\bullet}_{OH},H^{\bullet}_{i})^{\times}$. Such a charge-compensation mechanism was proposed in Refs. 5–9. However, since the calculated equilibrium concentration for the defect complex is quite small (see Fig. 13), it can be said from the present results that formation of $(V''_{Ca},V^{\bullet}_{OH},H^{\bullet}_{i})^{\times}$ in HAp is unlikely.

Finally, from the calculated concentrations of defect complexes, the Ca/P molar ratio of HAp as a function of pH is evaluated in Fig. 15. As shown in Fig. 13, the concentration of $(H'_{Ca\text{-}2c},H^{\bullet}_{i\text{-}1})^{\times}$ is much larger (by more than ten orders of magnitude) than those of the other complexes, and also the formation energy of PO_4^{3-} vacancies is too high to contribute to loss of phosphorous in the entire pH range (Fig. 11). As a result, it is found that the variation of Ca/P ratio is determined mostly by loss of calcium ions due to the formation of $(H'_{Ca\text{-}2},H^{\bullet}_{i\text{-}1})^{\times}$ at the Ca-2abc sites. In order to obtain Fig. 15, the defect complexes of $(H'_{Ca\text{-}2a},H^{\bullet}_{i\text{-}1})^{\times}$ and $(H'_{Ca\text{-}2b},H^{\bullet}_{i\text{-}1})^{\times}$ are also separately calculated. It is confirmed that they have almost identical defect configurations with $(H'_{Ca\text{-}2c},H^{\bullet}_{i\text{-}1})^{\times}$and the formation-energy difference is within 0.03 eV. This can be imagined from the similarity of structural and chemical environments of Ca-2a, Ca-2b, and Ca-2c sites.

In Fig. 15, the Ca/P ratio starts to lower at pH=7.5 from the stoichiometric value of Ca/P=1.67, and decreases with decreasing pH. It can be seen that experimental data by Zawacki *et al.*,[41] obtained from HAp precipitates from the supersaturated solution with respect to HAp, also shows the

TABLE III. Interatomic distances and bond angles around protons in the defect complexes, which are obtained from the optimized structures in Fig. 14 and are listed in the similar way to Table II.

Defect	O-H^* length (nm)	O···O distance (nm)	∠H^*-O···O (deg.)
$(H'_{Ca\text{-}2c},H^{\bullet}_{i\text{-}1})^{\times}$	0.102	0.261	11.3
	0.102	0.269	10.3
	(0.099)	(0.308)	(6.5)
$(V''_{Ca\text{-}1},2H^{\bullet}_{i})^{\times}$	0.098	0.363	24.9
	0.098	0.339	22.8
$(H'_{Ca\text{-}2c},V^{\bullet}_{OH})^{\times}$	0.103	0.270	12.6

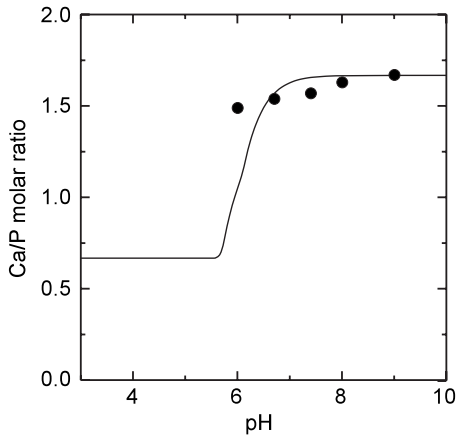

FIG. 15. pH dependence of Ca/P molar ratio in HAp. Filled circles indicate experimental data by Zawacki *et al.* (Ref. 41).

similar trend of decrease in Ca/P ratio against pH.

It is noted here that the Ca/P ratio becomes constant (0.67) at pH of less than about 5.5. This is because the formation energy of $(H'_{Ca\text{-}2}, H^{\bullet}_{i\text{-}1})^{\times}$ becomes negative at that pH, indicating that Ca-2 ions can be completely replaced by protons. In contrast, the concentration of $(V''_{Ca\text{-}1}, 2H^{\bullet}_{i})^{\times}$ is still too small to contribute to the Ca deficiency of HAp [Fig. 13(b)]. The constant Ca/P value of 0.67 indicates that Ca-1 and Ca′-1 ions remain in the HAp lattice even at such a low pH.

When the Ca-2 ions are completely missing at the low pH condition, it is thought that such highly defective HAp crystals are no longer stable and are easy to dissolve in the surrounding solution. In fact, it is reported that HAp exhibits increase in solubility with decreasing pH,[42–44] and that HAp minerals in naturally occurring teeth undergo rapid dissolution into plaque fluids around pH ≈5.5.[44] Based on the present theoretical results, it is speculated that these experimentally observed results and phenomena may be related to HAp instability due to the negative formation energy of $(H'_{Ca\text{-}2}, H^{\bullet}_{i\text{-}1})^{\times}$ in the low pH range.

Of course, HAp minerals in natural bones and teeth contain a variety of impurities that affect the crystal stability of HAp. In addition, surface chemistry of HAp, such as crystallography, surface termination and water adsorption, may play an important role for the defect stability and the resultant nonstoichiometry. In spite of such factors involved in real HAp, it is thought that the present first-principles approach represents some of salient features of complicated physics and chemistry in the biomaterials. Detailed impurity effects and surface effects in HAp properties will be addressed in near future.

IV. SUMMARY

First-principles calculations were performed for vacancies and protons in HAp, to investigate the dominant defect-formation mechanism inducing nonstoichiometry of HAp. As compared to intrinsic vacancies, interstitial and Ca-substituted protons tend to show smaller formation energies. The protons in HAp form H_2O^0 and HPO_4^{2-} by being bonded to adjacent OH^- and PO_4^{3-} groups and are stabilized by hydrogen bonding with neighboring PO_4^{3-} groups. In particular, the effect of defect association is significant, and the defect complexes of interstitial and Ca-substituted protons around the OH^- groups of the HAp lattice are easy to form in low pH conditions, even at the low temperature of 298 K. Then, it is found that the Ca/P molar ratios of HAp decrease with decreasing pH, which is in reasonable agreement with experiment.

ACKNOWLEDGMENTS

This work was supported by a Grant-in-Aid for Scientific Research from the Ministry of Education, Sports, Science and Culture of Japan. The author also acknowledges I. Tanaka for his support of computation.

[1] J. C. Elliot, *Structure and Chemistry of the Apatites and Other Calcium Orthophosphates* (Elsevier Science, Amsterdam, 1994).
[2] A. S. Posner and A. J. Perloff, J. Res. Natl. Bur. Stand. **58**, 279 (1957).
[3] A. S. Posner, J. M. Stutman, and E. R. Lippincott, Nature (London) **188**, 486 (1960).
[4] J. M. Stutman, A. S. Posner, and E. R. Lippincott, Nature (London) **193**, 368 (1962).
[5] L. Winand, M. J. Dallemagne, and G. Duyckaerts, Nature (London) **190**, 164 (1961).
[6] L. Winand and M. J. Dallemagne, Nature (London) **193**, 369 (1962).
[7] E. E. Berry, J. Inorg. Nucl. Chem. **29**, 317 (1967).
[8] E. E. Berry, J. Inorg. Nucl. Chem. **29**, 1585 (1967).
[9] G. Kuhl and W. H. Nebergall, Z. Anorg. Allg. Chem. **324**, 313 (1963).
[10] L. Calderín, M. J. Stott, and A. Rubio, Phys. Rev. B **67**, 134106 (2003).
[11] P. Rulis, L. Ouyang, and W. Y. Ching, Phys. Rev. B **70**, 155104 (2004).
[12] D. U. Schramm, J. Terra, A. M. Rossi, and D. E. Ellis, Phys. Rev. B **63**, 024107 (2000).
[13] M. Jiang, J. Terra, A. M. Rossi, M. A. Morales, E. M. Baggio Saitovitch, and D. E. Ellis, Phys. Rev. B **66**, 224107 (2002).
[14] J. Terra, M. Jiang, and D. E. Ellis, Philos. Mag. A **82**, 2357 (2002).
[15] R. Astala and M. J. Stott, Chem. Mater. **17**, 4125 (2005).
[16] R. Astala, L. Calderín, X. Yin, and M. J. Stott, Chem. Mater. **18**, 413 (2006).
[17] K. Matsunaga and A. Kuwabara, Phys. Rev. B **75**, 014102 (2007).
[18] G. Kresse and J. Furthmüller, Phys. Rev. B **54**, 11169 (1996).
[19] G. Kresse and J. Furthmüller, Comput. Mater. Sci. **6**, 15 (1996).
[20] P. E. Blöchl, Phys. Rev. B **50**, 17953 (1994).

[21] G. Kresse and D. Joubert, Phys. Rev. B **59**, 1758 (1999).
[22] J. P. Perdew, K. Burke, and M. Ernzerhof, Phys. Rev. Lett. **77**, 3865 (1996).
[23] J. C. Elliot, Science **180**, 1055 (1973).
[24] M. I. Kay, R. A. Young, and A. S. Posner, Nature (London) **204**, 1050 (1964).
[25] H. J. Monkhorst and J. D. Pack, Phys. Rev. B **13**, 5188 (1976).
[26] K. Matsunaga, T. Tanaka, T. Yamamoto, and Y. Ikuhara, Phys. Rev. B **68**, 085110 (2003).
[27] S. B. Zhang, S. H. Wei, A. Zunger, and H. Katayama-Yoshida, Phys. Rev. B **57**, 9642 (1998).
[28] A. F. Kohan, G. Ceder, D. Morgan, and Chris. G. Van de Walle, Phys. Rev. B **61**, 15019 (2000).
[29] I. G. Batyrev, A. Alavi, and M. W. Finnis, Phys. Rev. B **62**, 4698 (2000).
[30] J. R. Pliego Jr. and J. M. Riveros, Chem. Phys. Lett. **332**, 597 (2000).
[31] J. Llano and L. A. Eriksson, J. Chem. Phys. **117**, 10193 (2002).
[32] The NBS Tables of Chemical Thermodynamic Properties [J. Phys. Chem. Ref. Data **11**, 1 (1982)].
[33] J. E. Bartmess, J. Phys. Chem. **98**, 6420 (1994).
[34] R. W. G. Wycoff, *Crystal Structures* (Wiley, New York, 1963), Vol. 1.
[35] J. Donohue, *The Structures of Elements* (Wiley, New York, 1974).
[36] M. W. Chase Jr., *NIST-JANAF Thermochemical Tables*, 4th ed. (The American Institute of Standards and Technology, New York, 1998).
[37] R. M. H. Verbeeck, H. Steyaert, H. P. Thun, and F. Verbeek, J. Chem. Soc., Faraday Trans. 1 **76**, 209 (1980).
[38] S. Chander and D. W. Fuerstenau, J. Colloid Interface Sci. **70**, 506 (1979).
[39] J. C. Elliott, Calcif. Tissue Res. **3**, 293 (1969).
[40] G. Pálinkás, P. Bopp, G. Jancsó, and K. Heinzinger, Z. Naturforsch., A: Phys. Sci. **39**, 179 (1984).
[41] S. J. Zawacki, J. C. Heughebaert, and G. H. Nancollas, J. Colloid Interface Sci. **135**, 33 (1990).
[42] J. D. B. Featherstone, Community Dent. Oral Epidemiol. **27**, 31 (1999).
[43] R. M. H. Verbeeck, H. P. Thun, and F. C. M. Driessens, Z. Phys. Chem., Neue Folge **119**, 79 (1980).
[44] C. Dawes, J. Can. Dent. Assoc. **69**, 722 (2003).